ARTICLES
https://doi.org/10.1038/s41566-020-00701-x

nature photonics

Broadband Mie driven random quasi-phase-matching

Romolo Savo[1]✉, Andrea Morandi[1], Jolanda S. Müller[1], Fabian Kaufmann[1], Flavia Timpu[1], Marc Reig Escalé[1], Michele Zanini[2,3], Lucio Isa[2] and Rachel Grange[1]

High-quality crystals without inversion symmetry are the conventional platform to achieve optical frequency conversion via three-wave mixing. In bulk crystals, efficient wave mixing relies on phase-matching configurations, while at the micro- and nanoscale it requires resonant mechanisms that enhance the nonlinear light–matter interaction. These strategies commonly result in wavelength-specific performances and narrowband applications. Disordered photonic materials, made up of a random assembly of optical nonlinear crystals, enable a broadband tunability in the random quasi-phase-matching regime and do not require high-quality materials. Here, we combine resonances and disorder by implementing random quasi-phase-matching in Mie resonant spheres of a few micrometres realized by the bottom-up assembly of barium titanate nanocrystals. The measured second-harmonic generation reveals a combination of broadband and resonant wave mixing, in which Mie resonances drive and enhance the second-harmonic generation, while the disorder keeps the phase-matching conditions relaxed. Our nanocrystal assemblies provide new opportunities for tailored phase matching at the microscale, beyond the coherence length of the bulk crystal. They can be adapted to achieve frequency conversion from the near-ultraviolet to the infrared ranges, are low cost and can cover large surface areas.

Nonlinear optical processes of the second order—mediated by a $\chi^{(2)}$ susceptibility—are the common means to obtain coherent light at wavelengths not available with laser sources[1] and have become a reliable way to generate photon quantum states[2]. Applications are relevant in spectroscopy[3,4], bioimaging[5], ultrafast optics[6] and quantum photonics[7], making these nonlinear processes key to the development of near-future photonic technology. Non-centrosymmetric crystals, which lack inversion symmetry, are among the most attractive materials with second-order nonlinearity, thanks to high $\chi^{(2)}$ coefficients, wide transparency windows (visible to near-infrared) and high damage thresholds[8]. As known, their use is bounded by optical dispersion, which imposes strict phase-matching conditions to achieve optimal nonlinear conversion. Many methods have been developed for phase-matching control, such as phase matching in birefringent crystals[1], quasi-phase-matching[9], and modal[10] and cyclic[11] phase matching. Strategies to enhance the nonlinear processes at scales smaller than the coherence length of the crystal are also available, such as cavity coupling[12,13], vanishing-permittivity materials[14], and plasmonic and dielectric nanoresonators[15]. In all cases, the optimization of the nonlinear processes is based on an underlying resonant mechanism, providing wavelength-specific performances that hamper the use of $\chi^{(2)}$ crystalline devices for broadband, widely tunable applications.

Increasing the complexity of the nonlinear crystal structure leads to relaxed phase-matching conditions and to largely improved performances in broadband nonlinear mixing[16]. In the case of a fully disordered crystal, characterized by polydispersed and randomly arranged non-centrosymmetric crystalline domains, the amplitudes and phases of the mixed waves get randomized, so that interference terms average out and the nonlinear signal accumulates as the sum of the intensities generated from each domain. This three-wave mixing regime is known as random quasi-phase-matching (RQPM)[17–19] and so far it has been implemented in disordered polycrystals with micrometre-sized domains (10–100 μm)[17,20,21]. Its distinctive feature is the linear scaling of the nonlinear generated power with the number of domains, over distances larger than the coherence length and without any geometric constraints[17]. The disordered distribution of the crystalline domains also enables a flat broadband tunability of the wave mixing, due to the absence of resonant optimization mechanisms, as demonstrated in naturally grown crystals with a two-dimensional disorder[22,23].

An unexplored aspect, which we address here, is the use of non-centrosymmetric crystalline nanodomains to realize miniature $\chi^{(2)}$ disordered structures with a controlled geometry. This way, the system could sustain geometric resonances that enhance the nonlinear wave-mixing, similarly to crystalline micro-[24] and nanoresonators[25], simultaneously showing relaxed phase-matching conditions and a broadband tunability thanks to RQPM. The use of nanodomains is further motivated by the availability of metal-oxide nanocrystals with bulk $\chi^{(2)}$ properties[26,27], which allows for the bottom-up fabrication of $\chi^{(2)}$ disordered structures with an a priori control over the domain size distribution. So far, RQPM in nanostructured disorder has not been reported, and theory predicts no limitations on the possible domain size[19]. Attention has been dedicated to three-wave mixing in turbid crystalline nanopowders[28], but only in the multiple scattering regime[29,30]. Resonant enhancement of RQPM has been observed in a large optical-parametric-oscillator cavity[21], but never at the microscale.

Here, we realize three-dimensional $\chi^{(2)}$ disordered microspheres by the bottom-up assembly of barium titanate ($BaTiO_3$) nanocrystals and demonstrate their second-harmonic generation (SHG) through RQPM. This is identified by the linear scaling of the SHG power with the volume of the microstructures, over four orders of magnitude, reaching sizes six times larger than the coherence length of $BaTiO_3$. Thanks to the homogeneity in their refractive

[1]Optical Nanomaterial Group, Institute for Quantum Electronics, Department of Physics, ETH Zurich, Zurich, Switzerland. [2]Laboratory for Soft Materials and Interfaces, Department of Materials, ETH Zurich, Zurich, Switzerland. [3]FenX AG, Zurich, Switzerland. ✉e-mail: savor@phys.ethz.ch

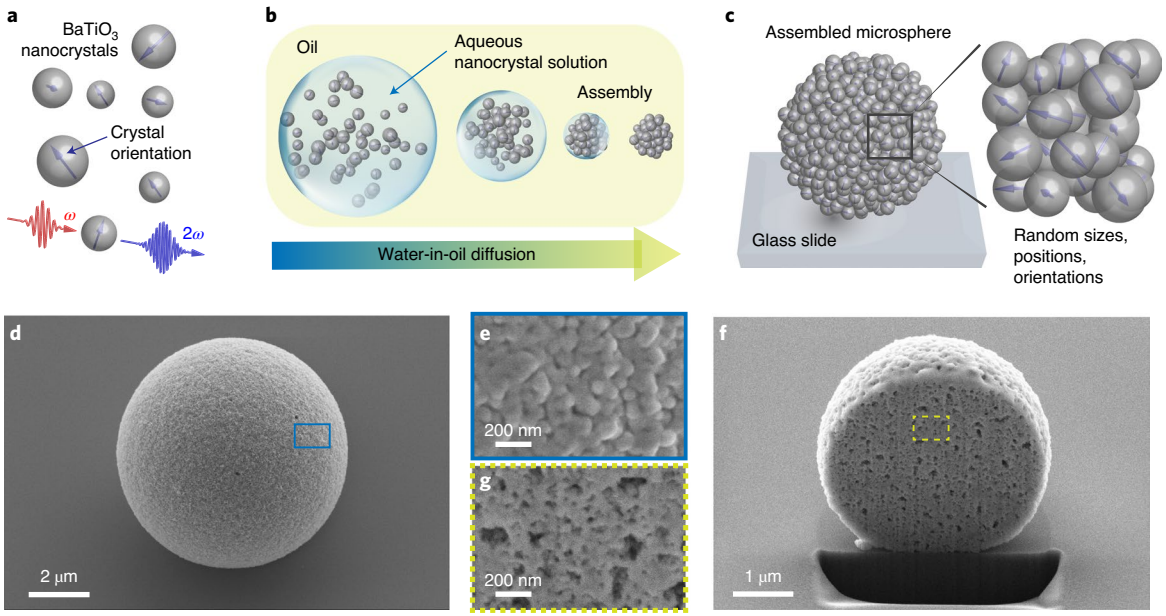

Fig. 1 | Bottom-up assembly of $BaTiO_3$ disordered microspheres. a, Schematic of the $BaTiO_3$ nanocrystals used in the assembly procedure. Their SHG efficiency depends on the size and orientation of the crystal, indicated by the arrows. **b**, Schematic of the emulsion-templated assembly procedure. **c**, Schematic of an assembled microsphere highlighting the randomness in the sizes, positions and orientations of the nanocrystals. **d**, SEM image of a $BaTiO_3$ microsphere assembled on a silicon substrate for better image quality. **e**, Close-up of the surface of the microsphere highlighting the disordered arrangement of the crystalline nanodomains. **f**, SEM image of the cross-section of a $BaTiO_3$ microsphere obtained by focused ion beam (FIB) milling. **g**, Close-up of the disordered, nanoporous inner structure of the microsphere.

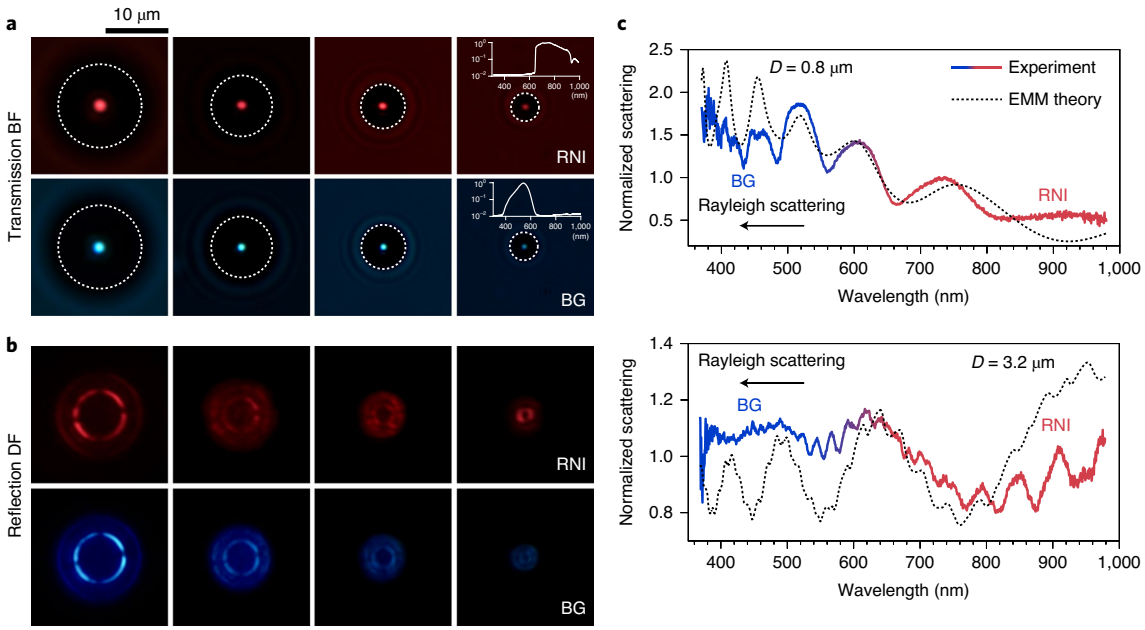

Fig. 2 | Linear optical characterization of the assembled microspheres. a, Optical microscopy images of individual microspheres of different sizes illuminated with red-near-infrared (RNI) and blue–green (BG) incoherent light. Images were acquired in transmission with a bright-field (BF) configuration and are in true colours. The two illuminations were obtained by filtering the light of the halogen lamp of the microscope. The corresponding spectra are shown as insets in the last images on the right, reporting the normalized intensity at different wavelengths. The white dotted lines indicate the contours of the microspheres. The spots in the centres correspond to the focusing of the illumination light. **b**, Images of the same microspheres shown in **a** acquired in reflection with a dark-field (DF) configuration, under RNI and BG illumination. The crossed rings in the centres are images of the DF illumination source. **c**, Light scattering spectra for two microspheres of different diameters D, measured in the DF configuration and with no filters for the illumination, that is, with white light. The red and blue parts of the experimental lines correspond to wavelengths falling within the RNI and the BG ranges. Experiments are fitted with the EMM model. Best-fit curves correspond to a filling fraction of 52% for $D = 0.8$ μm and 55% for $D = 3.2$ μm. For both curves, the absorption coefficient was set to $k = 0.003$. The arrows indicate the wavelengths at which Rayleigh scattering on the nanocrystals appears.

index, assembled microspheres sustain high-order Mie resonances stemming from their outer geometry, which couple to the RQPM mechanism and drive the SHG. Sweeping of the pump wavelength over a 100 nm range reveals a modulated SHG, resulting from a unique combination of broadband and resonant wave-mixing. This new regime of RQPM is described accurately by a random walk in the SHG complex plane whose step lengths depend on the local field enhancement within the microspheres. Theory shows that the Mie modes enhance the SHG by one order of magnitude. The microspheres are as efficient as crystalline $BaTiO_3$ of the same size by using 71% less material, with the further advantages of exhibiting a monotonic growth with the size, and relaxed phase-matching conditions for the direction and the polarization of the pump beam. We have realized a new class of nonlinear $\chi^{(2)}$ resonators by the bottom-up assembly of nanocrystals, providing evidence and modelling of an unexplored phase-matching regime, in which RQPM and Mie resonances couple together. Our systems are low cost and easily scalable to large surface areas, opening up possibilities of new designs for broadband and tunable nonlinear photonic devices based on disorder.

Results

Bottom-up assembly of $\chi^{(2)}$ disordered $BaTiO_3$ microspheres. We realized micrometre-sized spherical structures by the emulsion-templated assembly[31,32] of colloidal $BaTiO_3$ nanocrystals (mean diameter 50 nm, 5% polydispersity). As previously empirically confirmed[33], the synthetic nanocrystals are characterized by a crystallographic tetragonal phase enabling bulk SHG at the nanoscale under femtosecond pulsed illumination[15,27] (Fig. 1a). We developed an assembly procedure (see Methods) in which the aqueous dispersion (2 wt%) of $BaTiO_3$ nanocrystals is mixed with surfactant-loaded (SPAN80 1 wt%) hexadecane and emulsified by mechanical shaking to generate polydispersed water-in-oil droplets (Fig. 1b). Water evaporation through the hexadecane reduces the size of the droplets and the water/oil interfaces act as dynamic templates for the assembly of the nanocrystals into larger microspheres. Assemblies were finally deposited on a glass substrate (Fig. 1b,c). Their size distribution depends on the size dispersion of the droplets and on the concentration of the nanocrystals in water. We generated microspheres with diameters from 0.5 µm to 20 µm. Assembled structures have a purely spherical geometry (Fig. 1d) over the whole size range (Supplementary Section 2). The surface roughness is solely determined by the finite size of the nanocrystals. A close-up of the microsphere surface is shown in Fig. 1e, where the crystalline polydispersed nanodomains are clearly visible. Owing to Brownian motion and the polydispersity, the nanocrystals assemble with random orientations and positions (Fig. 1c). The microsphere cross-section (Fig. 1f,g) reveals a disordered nanoporous structure with a filling fraction of 55%, measured by image analysis (Supplementary Section 3). The microspheres are not sintered and the nanocrystals are bound by surface forces. Remarkably, they are robust and appear free from deformation several months after fabrication.

Linear effective medium Mie behaviour. The linear optical properties of the assembled microspheres were investigated with an upright microscope customized for spectral measurements (Supplementary Section 4). In Fig. 2a,b, microspheres of different sizes have been illuminated with red-near-infrared and blue–green incoherent light to probe their clear appearance in the spectral regions of the pump and of the SHG wavelength, respectively. The images show that the microspheres function as microlenses and provide evidence that the nanocrystal–air composite behaves as an effective medium. In Fig. 2a, the microspheres focus light in transmission, showing sharp foci over empty backgrounds, for all sizes and under both types of illumination. In reflection (Fig. 2b), the same microspheres create

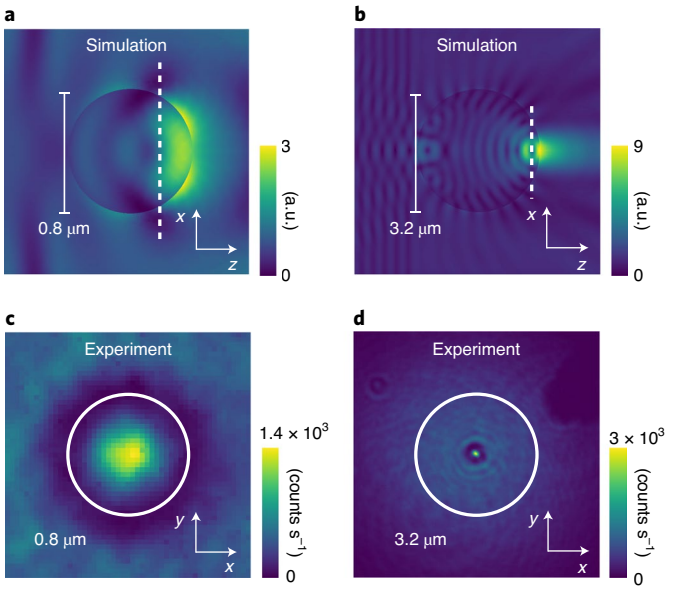

Fig. 3 | Simulation and visualization of the linear quasi-normal modes of the microspheres. a, FEM simulation in the effective medium approximation of the linear modes excited by a plane wave (coming from the left) at 930 nm in a microsphere with a diameter $D = 0.8$ µm. The colour pattern indicates the amplitude distribution of the modes in the x–z plane. **b**, FEM simulation as in **a** for a microsphere with $D = 3.2$ µm. **c**, Experimental image of the rear plane of a microsphere with $D = 0.8$ µm obtained with laser light at 930 nm. The colour pattern indicates the measured power. The line indicates the countour of the microsphere, whose diameter has been measured by an SEM. The plane of this image is orthogonal to the one simulated in **a**, where it is indicated by the white dashed line. **d**, Experimental image as in **c** for a microsphere with $D = 3.2$ µm. The plane of this image is indicated in **b** by the white dashed line.

the image of the illumination source[34]. A faint background halo is observable under blue–green illumination, which can be attributed to residual Rayleigh scattering on the nanocrystals. As shown, this Rayleigh scattering is weak and does not compromise the clear appearance of the structure.

To identify resonant scattering due to the spherical shape, scattering spectra from individual microspheres were measured under white illumination in a dark-field configuration. Spectra are shown in Fig. 2c for two different diameters. Distinct resonances are observed, which get spectrally denser for the larger diameter, since higher-order modes are excited. This shows that the microspheres act as optical Mie resonators[35]. To describe the observation and to unambiguously relate it to the spherical geometry of the assembly, we modelled the microspheres as homogeneous spheres with the same size and with an effective refractive index. Then, we calculated the scattering cross-section with Mie theory. We refer to this description as an effective medium Mie (EMM) model (see Methods and Supplementary Section 5). Theoretical curves are plotted over the data in Fig. 2c. The agreement with the experiments in the red-near-infrared spectral region supports the Mie resonator description. The EMM model estimates an effective refractive index $n_{\mathrm{eff}} \approx 1.55$ and highlights the widening of the resonances that are due to the presence of the substrate, which we have taken into account by adding an imaginary part to n_{eff} (see Methods and Supplementary Section 5). In the blue–green spectral region, the agreement is qualitative and only the positions of the peaks can be described. The deficiency of the EMM model at shorter wavelengths can be attributed to the weak Rayleigh scattering observed

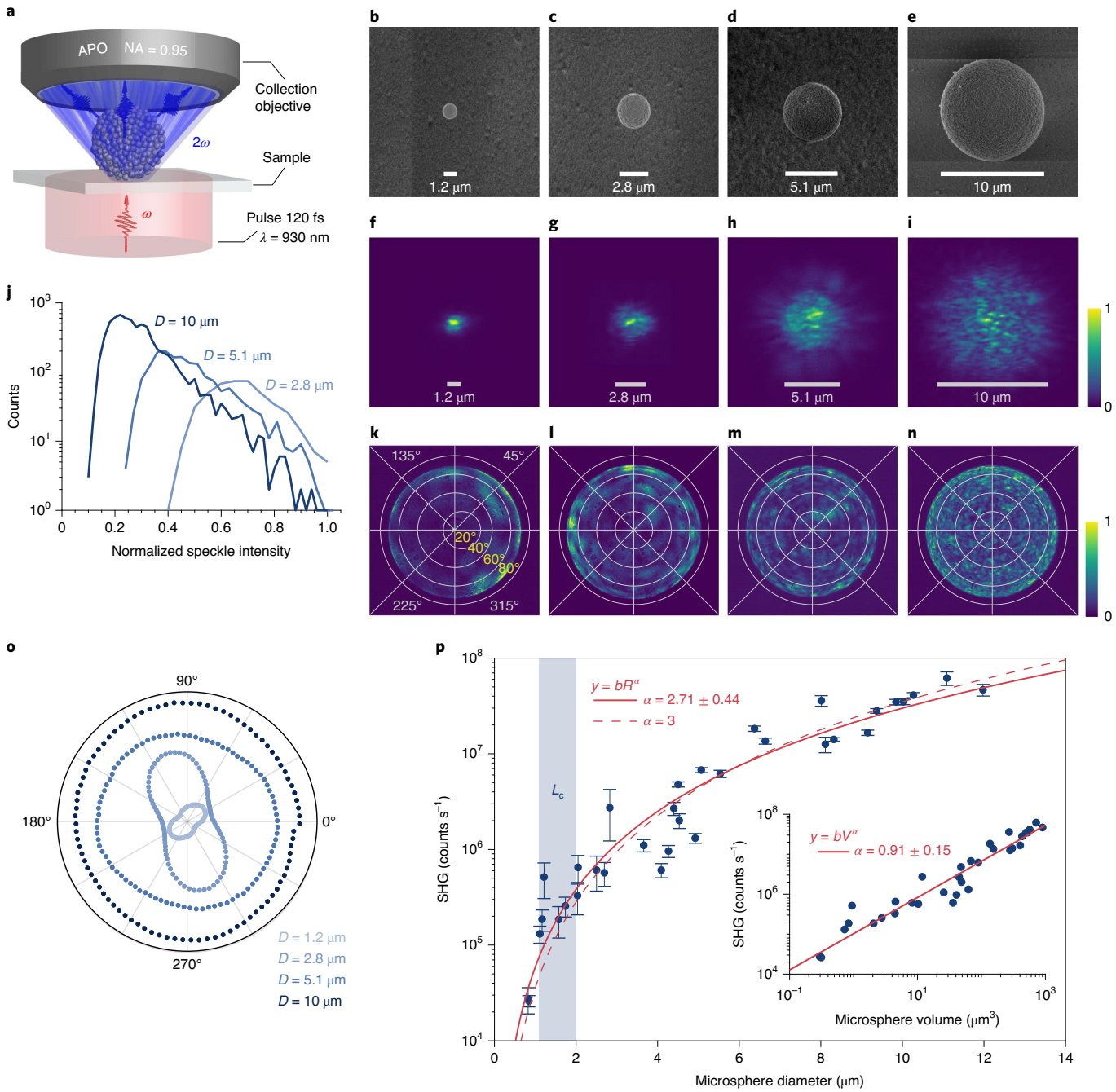

Fig. 4 | SHG from the assembled microspheres and observation of RQPM. a, Schematic of the experimental configuration for the nonlinear characterization of individual microspheres. APO, apochromat. **b**–**e**, SEM images of four microspheres with increasing size assembled on a glass substrate. Diameters are indicated. **f**–**i**, Images of the SHG emitted from the microspheres shown in **b**–**e**. Correspondence is along the column. The focal plane of the objective is placed in the central section of the structures. Reported sizes are measured from the image after calibration of the camera. The colour scale indicates the normalized power. **j**, Statistical intensity distributions for the speckles in **g**–**i**. The *y* axis is in log scale. **k**–**n**, Images of the back focal plane of the objective for the SHG shown in **f**–**i**. Correspondence is along the column. The colour scale indicates the normalized power. **o**, SHG power integrated over the entire speckle image for a variable input polarization. Measurements are performed on the microspheres in **b**–**e**. Single curves are normalized to avoid overlapping. **p**, The SHG from a set of 32 microspheres with increasing diameter, integrated over the entire speckle image, and averaged over the input polarization. Error bars report the range of variability when rotating the input polarization. The red lines are fits obtained with the power law $y = bR^{\alpha}$, with b and α free parameters (solid line), with b free parameter and $\alpha = 3$ (dashed line). The blue region indicates the range of variability of the coherence length (L_c) of crystalline $BaTiO_3$ at 930 nm. The inset shows the scaling of the SHG power with the volume, V, of the microsphere. The red line is a fit with the power law $y = bV^{\alpha}$, with b and α free parameters. The errors on α correspond to a confidence interval of 99.7% (3σ).

in Fig. 2b. The largest microsphere may also suffer from a partial collection of the Mie scattered light, due to the limited field of view of the dark-field configuration (≈4 μm).

The quasi-normal modes[36] of the two microspheres were computed by finite-element method (FEM) simulations in the effective medium approximation for the pump wavelength (930 nm)

(Fig. 3a,b). The pronounced mode confinement opposite to the wide illumination is known as a photonic nanojet[37] and it corresponds to the focused light observed in Fig. 2a. The conditions of the simulations were created experimentally by illuminating the microspheres with coherent light at 930 nm and by imaging their rear plane. We used the set-up shown in Fig. 4a, collecting only the pump light. As shown in Fig. 3c,d, the nanojet is observed in both microspheres, with spatial features that match the simulated ones. Since the nanojet can be derived by Mie theory[38], both the resonant and the focusing properties observed experimentally corroborate the EMM behaviour of the microspheres in the linear regime.

SHG through RQPM. The SHG was measured on a set of 32 microspheres having diameters between 1–12 μm, by illuminating them with pulses of 120 fs at 930 nm (ω, the pump frequency) in the configuration shown in Fig. 4a (see Methods and Supplementary Section 6). The spectrum and the quadratic power-dependence of the measured nonlinear signal prove the SHG at 465 nm (2ω) (Supplementary Section 7). Scanning electron microscope (SEM) images of four microspheres with different diameters are shown in Fig. 4b–e and are considered as prototype examples to study the size-dependent properties of the SHG. The images of the SHG reveal speckle patterns due to the $\chi^{(2)}$ disorder (Fig. 4f–i) in contrast with the effective medium behaviour observed in the linear regime. SHG simulations from disordered assemblies of $BaTiO_3$ nanocrystals corroborate this observation. They reveal that the size and the orientation of the nanocrystal have a substantial influence on the amplitude and the phase of the SHG. As a consequence, the structural disorder creates multiple waves at 2ω with random phase and amplitude, which interfere and generate the speckle. The weak scattering at 2ω is modelled as an additional phase randomization and this does not affect the SHG efficiency (Supplementary Section 8.5).

Figure 4f–i shows that the SHG comes from the entire microsphere, with a size and a symmetry that match those of the corresponding structures. The nonlinear signal appears more efficient in the centre of the image, as a consequence of the spherical shape and consistently with the focusing of the pump in a nanojet (Fig. 3). As shown in Fig. 4k–n, the SHG is broadly and isotropically distributed over the solid angle of collection (≈75°), over an angular range broader than the one calculated for the pump by using the EMM theory (<30°) (Supplementary Section 5.3). This angular dispersion might be used to decouple the generated harmonic from the pump without the use of filters[39]. The efficiency is comparable along the different directions, with a more distinct emission at very large azimuthal angles (>60°). This may be due to the isotropic SHG emission from each nanocrystal or due to the weak SHG scattering. Further investigation is necessary, in particular on the influence of the multiscale structure of the microsphere on the SHG angular pattern, since this aspect is not considered in the numerical model.

The statistical intensity distributions of the speckles are shown in Fig. 4j for the three largest microspheres. The observed Rayleigh distributions provide evidence of SHG interference from a large number of fully randomized emitters, without dominant orientation or position correlations[40]. The rounding of the distributions at low intensities is due to the acquisition of both output polarizations. The more pronounced exponential tail for increasing diameters is due to the larger statistics available. Also, the SHG measured at variable input polarization confirms the random nature of the $\chi^{(2)}$ disorder (Fig. 4o). Large microspheres ($D > 5$ μm) show a fully isotropic response, corresponding to the absence of polarization selection rules. At smaller sizes ($D < 5$ μm), a residual polarization dependence is observed. This effect becomes clear by combining FEM simulations to compute the pump mode and the numerical model to calculate the SHG (Supplementary Section 8). We found that 50% of the SHG power comes from the 1–2% fraction of the volume

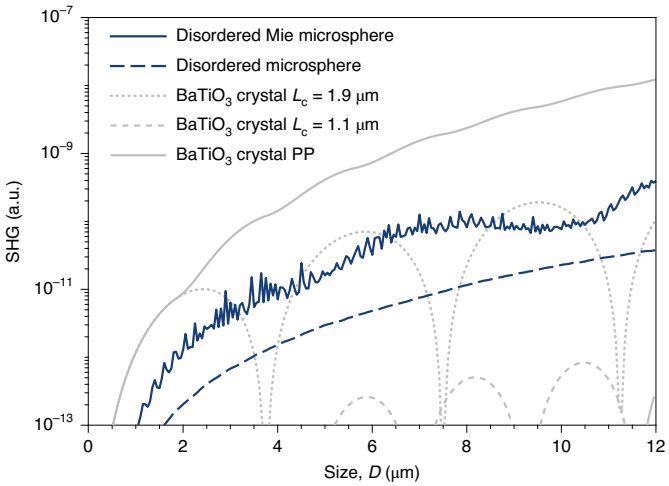

Fig. 5 | Numerical comparison of the SHG scaling between the disordered microspheres and $BaTiO_3$ crystalline structures. The blue lines indicate the SHG power of disordered microspheres calculated with (solid) and without (dashed) the Mie enhancement. Calculations consider nanocrystals with a mean size of 50 nm, 5% polydispersity and a 55% filling fraction. The size D indicates the microsphere diameter. The grey lines are the efficiency of $BaTiO_3$ single crystals with a randomly chosen coherence length L_c (dashed) and the maximal coherence length L_c (dotted). The periodically poled (PP) crystal (solid) has the maximal coherence length, and the polarity is flipped at every coherence length to compensate the phase mismatch. This corresponds to a quasi-phase-matched crystal and represents the most efficient option for $BaTiO_3$. Calculations for the crystalline structures consider a cuboid shape and no resonant effects. The size D indicates the side length. Owing to their spherical shape and their filling fraction, the microspheres have 29% of the material of the crystalline structures. The data shown here are reported in terms of the SHG efficiency in Supplementary Section 8.

corresponding to the nanojet. For smaller sizes, this contribution is characterized by a partial averaging of the random interference and introduces the visible polarization dependence (Supplementary Section 8). Interestingly, this polarization dependence is still relaxed, with a variability of 20% on average. A similar effect has been observed in Au/ZnO nanostructures[41]. The phase-matching properties are investigated in Fig. 4p. The SHG scaling is measured on microspheres whose diameters reach values six times larger than the maximal coherence length of $BaTiO_3$ (Supplementary Section 1). Power-law fitting of the data returns a best-fit exponent $\alpha = 2.71 \pm 0.44$, which is compatible with $\alpha = 3$ and demonstrates the presence of RQPM. The data correspond to a linear scaling with the volume of the microspheres, that is, with the number of the nanocrystals, over four orders of magnitude as shown in the inset of Fig. 4p. The large uncertainty on the scaling exponent stems from the vertical dispersion of the data, whose origin lies in the resonant properties of the microspheres.

Coupling to Mie resonances. To account for resonant effects, the RQPM model (Supplementary Section 8) was extended to $\chi^{(2)}$ disordered structures sustaining modes. In this case, the total SHG field is the result of a random walk in the complex plane of the SHG field, with a mode-dependent step-length distribution, as shown in Supplementary Fig. 15. The SHG power is given by the variance of this random walk and reads

$$P_{\mathrm{SHG}}(R,\omega,2\omega) = \eta(\chi^{(2)}_{\mathrm{eff}}\omega)^2 N(R) I_\omega^2 \times \overline{\xi^2}(R,\omega,2\omega), \qquad (1)$$

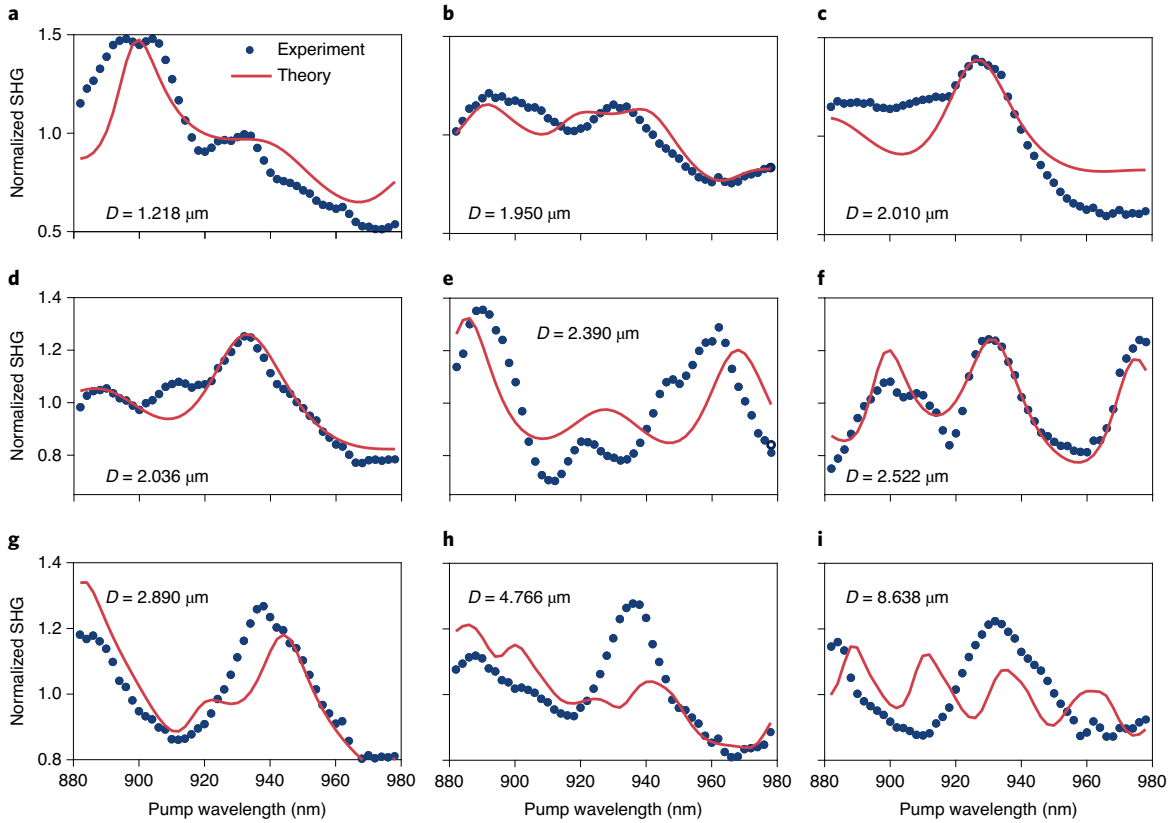

Fig. 6 | Wavelength-dependent Mie driven SHG from the assembled microspheres. a–i, The SHG power measured from microspheres of different diameters obtained by sweeping the pump wavelength between 880–980 nm together with the best-fit function obtained by using equation (1). Theoretical curves in **a**,**b** consider the enhancement from the Mie modes at ω and at 2ω. Theoretical curves in **c–i** consider the enhancement from the Mie modes only at ω. Losses due to outcoupling to the substrate are modelled with an absorption coefficient. Reported diameters have an error of ±20 nm. Values of the filling fractions and of the absorption coefficient returned by the fits are reported in Supplementary Section 9. Both experimental data and theory are normalized to their mean values.

where η is a proportionality factor that accounts for the RQPM efficiency for a given mean size and polydispersity of the nanocrystals, $\chi^{(2)}_{\mathrm{eff}}$ is the effective second-order susceptibility of the material, $N(R)$ is the number of nanocrystals within a microsphere of radius R, I_ω is the pump intensity, and $\overline{\xi^2}(R,\omega,2\omega)$ is the volume-averaged squared field enhancement of the Mie modes (see Methods and Supplementary Section 9).

The SHG scaling calculated with equation (1) is shown in Fig. 5. The model reproduces the general trend of the experiment, with the monotonic $\propto R^3$ scaling of RQPM and the Mie resonant fringes (solid blue line). Notably, the Mie modes introduce an overall SHG enhancement of one order of magnitude (dashed to solid blue line), which stems from both the increased mean energy and the focusing of the pump power in a small volume, that is, in the nanojet.

The figure of merit for the conversion in the RQPM regime is the comparison with crystalline non-resonant structures of the same size[17]. Since $BaTiO_3$ is a non-phase-matchable material[42], two different orientations were considered for the crystalline counterparts: an optimized orientation providing the longest possible coherence length (best oriented) and a random orientation corresponding to a non-specific coherence length (randomly oriented). As shown in Fig. 5, the SHG from the crystalline structures (dotted and dashed grey lines) destructively and constructively interfere in a periodic manner. When considering the Mie enhancement, the SHG from the microspheres is always comparable to the best-oriented crystals, with the important advantage of having their phase-matching conditions relaxed. Interestingly, the microspheres show a SHG that is two orders of magnitude stronger than the randomly oriented crystals (dashed grey line). This is a remarkable advantage, since controlling the lattice orientation, after or during the growth of the crystal, is a demanding task. To complete the comparison, we show the case of optimally oriented and periodically poled crystals (solid grey line). As expected, the periodically poled structures are more efficient than the disordered microspheres, but in practice they are hardly achievable due to the short coherence length of $BaTiO_3$ (ref. [42]). Even though the microspheres are extremely small and contain only 29% of the material of the crystals (see Fig. 5 caption), they are as efficient and appear to be a valid alternative to the crystalline counterparts. Absolute efficiencies are provided in Supplementary Section 8.4.

The wavelength-dependent SHG was measured on microspheres with increasing diameter, by sweeping the pump laser over a 100 nm wavelength range around 930 nm (Fig. 6). The SHG is tunable over the entire bandwidth, as expected by RQPM[22], and is additionally driven by the Mie resonances of the microspheres. This resonant modulation has the same origin as the fringes characterizing the SHG scaling. Equation (1) was employed within a fitting procedure, by using the microsphere filling fraction as the main free parameter. The good agreement with the measurements validates the model. For diameters larger than 2 μm (Fig. 6c–g), the fitting requires to consider the Mie modes at ω, neglecting those at 2ω. This is related to the calculation of the Mie modes with a plane-wave illumination and to the weak scattering at 2ω. The discrepancy observed for the largest diameters (Fig. 6h,i) may instead be attributed to an overestimation of the losses or to internal scattering at ω.

Conclusions

We have realized a multifunctional platform based on the bottom-up assembly of $BaTiO_3$ nanocrystals to study second-order nonlinear effects in disordered photonic materials. We observed an unexplored phase-matching mechanism that relies on the coupling of RQPM with the Mie resonances of the entire disordered structure. The assembled microspheres show a broadband and simultaneous Mie enhanced SHG over a wavelength range of 100 nm. We present an optimization mechanism for the SHG at scales larger than the coherence length that is not related to the orientation and the quality of the crystal, but that exploits the geometry of the structure. Our model describes the main observations well and pinpoints the essential physics from a complex interplay of linear and nonlinear effects.

This work opens the door to still uncharted research. Minimization of losses due to outcoupling to the substrate is of primary importance, and, for example, by introducing a spacer, would drastically improve the Mie resonant enhancement and potentially compensate for the weak efficiency of the nanodomains in comparison with the microdomains. Other research directions could be the use of near-field coupling to excite specific modes and the minimization of the internal scattering. Since the SHG is a coherent process, there is a whole set of opportunities provided by disorder to achieve tailored interference[43,44], both for the pump and the SHG. Interesting perspectives are the hierarchical assembling of monodispersed or bidispersed microspheres into large-scale correlated structures[45] and the implementation of wavefront-shaping protocols to control and optimize the efficiency and the bandwidth of the nonlinear processes[46,47]. Thanks to the cost-effective and scalable production of the microspheres, we envision applications in the fabrication of tunable wide-acceptance-angle up-conversion screens[48]. Owing to the time-reversal symmetry of the three-wave mixing process, the results provided here could be extended to spontaneous parametric down-conversion[21] and to the realization of disordered quantum sources.

Online content

Any methods, additional references, Nature Research reporting summaries, source data, extended data, supplementary information, acknowledgements, peer review information; details of author contributions and competing interests; and statements of data and code availability are available at https://doi.org/10.1038/s41566-020-00701-x.

Received: 5 March 2020; Accepted: 11 September 2020;
Published online: 12 October 2020

References

1. Boyd, R. W. *Nonlinear Optics* (Elsevier, 2008).
2. Kwiat, P. G. et al. New high-intensity source of polarization-entangled photon pairs. *Phys. Rev. Lett.* **75**, 4337–4341 (1995).
3. Shen, Y. R. A few selected applications of surface nonlinear optical spectroscopy. *Proc. Natl Acad. Sci. USA* **93**, 12104–12111 (1996).
4. Werner, C. S., Buse, K. & Breunig, I. Continuous-wave whispering-gallery optical parametric oscillator for high-resolution spectroscopy. *Opt. Lett.* **40**, 772–775 (2015).
5. Campagnola, P. J. & Loew, L. M. Second-harmonic imaging microscopy for visualizing biomolecular arrays in cells, tissues and organisms. *Nat. Biotechnol.* **21**, 1356–1360 (2003).
6. Trebino, R. *Frequency-Resolved Optical Gating: The Measurement of Ultrashort Laser Pulses* (Springer Science & Business Media, 2012).
7. Caspani, L. et al. Integrated sources of photon quantum states based on nonlinear optics. *Light Sci. Appl.* **6**, e17100 (2017).
8. Günter, P. *Nonlinear Optical Effects and Materials* Vol. 72 (Springer, 2012).
9. Fejer, M. M., Magel, G., Jundt, D. H. & Byer, R. L. Quasi-phase-matched second harmonic generation: tuning and tolerances. *IEEE J. Quant. Electron.* **28**, 2631–2654 (1992).
10. Moutzouris, K. et al. Second-harmonic generation through optimized modal phase matching in semiconductor waveguides. *Appl. Phys. Lett.* **83**, 620–622 (2003).
11. Lin, G., Fürst, J. U., Strekalov, D. V. & Yu, N. Wide-range cyclic phase matching and second harmonic generation in whispering gallery resonators. *Appl. Phys. Lett.* **103**, 181107 (2013).
12. Rivoire, K., Buckley, S. & Vučković, J. Multiply resonant photonic crystal nanocavities for nonlinear frequency conversion. *Opt. Express* **19**, 22198–22207 (2011).
13. Lin, Z., Liang, X., Lončar, M., Johnson, S. G. & Rodriguez, A. W. Cavity-enhanced second-harmonic generation via nonlinear-overlap optimization. *Optica* **3**, 233–238 (2016).
14. Suchowski, H. et al. Phase mismatch–free nonlinear propagation in optical zero-index materials. *Science* **342**, 1223–1226 (2013).
15. Pu, Y., Grange, R., Hsieh, C.-L. & Psaltis, D. Nonlinear optical properties of core-shell nanocavities for enhanced second-harmonic generation. *Phys. Rev. Lett.* **104**, 207402 (2010).
16. Suchowski, H., Bruner, B. D., Arie, A. & Silberberg, Y. Broadband nonlinear frequency conversion. *Opt. Photon. News* **21**, 36–41 (2010).
17. Baudrier-Raybaut, M., Haidar, R., Kupecek, P., Lemasson, P. & Rosencher, E. Random quasi-phase-matching in bulk polycrystalline isotropic nonlinear materials. *Nature* **432**, 374–376 (2004).
18. Skipetrov, S. E. Nonlinear optics: disorder is the new order. *Nature* **432**, 285–286 (2004).
19. Vidal, X. & Martorell, J. Generation of light in media with a random distribution of nonlinear domains. *Phys. Rev. Lett.* **97**, 013902 (2006).
20. Bravo-Abad, J., Vidal, X., Juárez, J. L. D. & Martorell, J. Optical second-harmonic scattering from a non-diffusive random distribution of nonlinear domains. *Opt. Express* **18**, 14202–14211 (2010).
21. Ru, Q. et al. Optical parametric oscillation in a random polycrystalline medium. *Optica* **4**, 617–618 (2017).
22. Fischer, R., Saltiel, S., Neshev, D., Krolikowski, W. & Kivshar, Y. S. Broadband femtosecond frequency doubling in random media. *Appl. Phys. Lett.* **89**, 191105 (2006).
23. Molina, P., de la O Ramírez, M. & Bausá, L. E. Strontium barium niobate as a multifunctional two-dimensional nonlinear 'photonic glass'. *Adv. Funct. Mater.* **18**, 709–715 (2008).
24. Ricciardi, I. et al. Frequency comb generation in quadratic nonlinear media. *Phys. Rev. A* **91**, 063839 (2015).
25. Kuznetsov, A. I., Miroshnichenko, A. E., Brongersma, M. L., Kivshar, Y. S. & Luk'yanchuk, B. Optically resonant dielectric nanostructures. *Science* **354**, aag2472 (2016).
26. Kim, E. et al. Second-harmonic generation of single $BaTiO_3$ nanoparticles down to 22 nm diameter. *ACS Nano* **7**, 5343–5349 (2013).
27. Timpu, F., Sergeyev, A., Hendricks, N. R. & Grange, R. Second-harmonic enhancement with Mie resonances in perovskite nanoparticles. *ACS Photonics* **4**, 76–84 (2016).
28. de Boer, J. F., Lagendijk, A., Sprik, R. & Feng, S. Transmission and reflection correlations of second harmonic waves in nonlinear random media. *Phys. Rev. Lett.* **71**, 3947–3950 (1993).
29. Faez, S., Johnson, P., Mazurenko, D. & Lagendijk, A. Experimental observation of second-harmonic generation and diffusion inside random media. *J. Opt. Soc. Am. B* **26**, 235–243 (2009).
30. Makeev, E. & Skipetrov, S. Second harmonic generation in suspensions of spherical particles. *Opt. Commun.* **224**, 139–147 (2003).
31. Kim, S.-H. et al. Microspheres with tunable refractive index by controlled assembly of nanoparticles. *Adv. Mater.* **20**, 3268–3273 (2008).
32. Vogel, N. et al. Color from hierarchy: diverse optical properties of micron-sized spherical colloidal assemblies. *Proc. Natl Acad. Sci. USA* **112**, 10845–10850 (2015).
33. Vogler-Neuling, V. V. et al. Solution-processed barium titanate nonlinear woodpile photonic structures with large surface areas. *Physica Stat. Solidi b* **257**, 1900755 (2020).
34. Yang, H., Moullan, N., Auwerx, J. & Gijs, M. A. Super-resolution biological microscopy using virtual imaging by a microsphere nanoscope. *Small* **10**, 1712–1718 (2014).
35. Checcucci, S. et al. Titania-based spherical Mie resonators elaborated by high-throughput aerosol spray: single object investigation. *Adv. Funct. Mater.* **28**, 1801958 (2018).
36. Lalanne, P., Yan, W., Vynck, K., Sauvan, C. & Hugonin, J.-P. Light interaction with photonic and plasmonic resonances. *Laser Photon. Rev.* **12**, 1700113 (2018).
37. Chen, Z., Taflove, A. & Backman, V. Photonic nanojet enhancement of backscattering of light by nanoparticles: a potential novel visible-light ultramicroscopy technique. *Opt. Express* **12**, 1214–1220 (2004).
38. Geints, Y. E., Zemlyanov, A. A. & Panina, E. K. Photonic jets from resonantly excited transparent dielectric microspheres. *J. Opt. Soc. Am. B* **29**, 758–762 (2012).
39. Molina, P. et al. Nonlinear prism based on the natural ferroelectric domain structure in calcium barium niobate. *Appl. Phys. Lett.* **94**, 071111 (2009).
40. Goodman, J. W. Some fundamental properties of speckle. *J. Opt. Soc. Am.* **66**, 1145–1150 (1976).

41. Zhong, J.-H. et al. Nonlinear plasmon-exciton coupling enhances sum-frequency generation from a hybrid metal/semiconductor nanostructure. *Nat. Commun.* **11**, 1464 (2020).
42. Setzler, S. et al. Periodically poled barium titanate as a new nonlinear optical material. In *Advanced Solid State Lasers* Paper MD1 (Optical Society of America, 1999).
43. Wiersma, D. S. Disordered photonics. *Nat. Photon.* **7**, 188–196 (2013).
44. Rotter, S. & Gigan, S. Light fields in complex media: mesoscopic scattering meets wave control. *Rev. Mod. Phys.* **89**, 015005 (2017).
45. Florescu, M., Torquato, S. & Steinhardt, P. J. Designer disordered materials with large, complete photonic band gaps. *Proc. Natl Acad. Sci. USA* **106**, 20658–20663 (2009).
46. Frostig, H. et al. Focusing light by wavefront shaping through disorder and nonlinearity. *Optica* **4**, 1073–1079 (2017).
47. Qiao, Y., Peng, Y., Zheng, Y., Ye, F. & Chen, X. Second-harmonic focusing by a nonlinear turbid medium via feedback-based wavefront shaping. *Opt. Lett.* **42**, 1895–1898 (2017).
48. Barh, A., Rodrigo, P. J., Meng, L., Pedersen, C. & Tidemand-Lichtenberg, P. Parametric upconversion imaging and its applications. *Adv. Opt. Photon.* **11**, 952–1019 (2019).

Methods

Emulsion-driven assembly. Barium titanate ($BaTiO_3$) nanocrystals were purchased from Nyacol Nano Technology Inc. (BT80 25% wt) as a stable aqueous dispersion. The emulsion was prepared by vigorously shaking by hand 10 µl of the dispersion (2% wt) mixed with 2.5 ml of surfactant-loaded hexadecane (SPAN80 1% wt). About 100 µl of the emulsified mixture was transferred onto a microscope glass slide before emulsion coalescence and was baked at 80 °C for 12 h in the oven. Glass slides were 1 mm thick. The deposited water/$BaTiO_3$ droplets were stable and tended to settle on a single layer over the slide. Complete water-into-hexadecane diffusion was already observed after 1 h of baking. The remaining heat treatment was necessary for the complete evaporation of the hexadecane. Residual surfactant was removed by sequentially washing with hexane. Since $BaTiO_3$ has a Curie temperature of 120 °C, the microspheres were not sintered. Exposing the nanocrystals to much higher temperatures could result in a non-reversible transition to the cubic crystalline phase and in the loss of non-centrosymmetry.

EMM model and fitting procedure. The EMM model first calculates the effective refractive index of the sphere through the Maxwell–Garnett mixing rule based on the average value of the ordinary and extraordinary refractive index of bulk $BaTiO_3$ ($n \approx 2.4$ at 600 nm) and on a variable filling fraction. This value of n_{eff} is used together with the diameter of the microspheres measured with the SEM to calculate the unpolarized scattering cross-section by using Mie theory for spherical particles. We took the specific illumination-collection geometry of the measurements into account. By varying the filling fraction of the microspheres between 45% and 65% and by fixing the absorption coefficient to $k = 0.003$, we created a dataset for the fitting procedure. Both experimental and theoretical spectra are normalized to their mean values. Best-fitting curves were selected by using the least-squares method. See Supplementary Section 5 for more details.

Effect of the substrate on Mie resonances. We simulated the scattering from a homogeneous sphere with effective refractive index $n_{\mathrm{eff}} = 1.55$ placed on a glass substrate and illuminated by a plane wave at 930 nm by using COMSOL. The results from the simulations are reported in Supplementary Section 5.3. These show that the substrate has little effect on the resonance positions, as it causes a shift of only a few nanometres. However, it introduces dominant outcoupling losses that smooth out the resonant peaks. In Supplementary Section 5.3 we show that the presence of the substrate can be included in the analytical EMM theory by adding an imaginary part to the effective refractive index, with absorption coefficients typically of $k \approx 0.005$.

Optical nonlinear set-up. The SHG from the microspheres was measured by free-space coupling the samples with linearly polarized laser pulses of 120 fs at 930 nm, with a repetition rate of 80 MHz. We set the waist (full-width at half-maximum) of the pump beam to 21 µm, which is larger than the microspheres, to approximate a plane-wave illumination. The average power of the train of pulses was 180 mW, corresponding to a single-pulse fluence of 0.68 mJ cm^{-2}. The SHG was collected in the forward direction with an apochromat (APO) high-numerical-aperture (NA) objective (NA = 0.95). The angular emission of the SHG was obtained by imaging the back focal plane (Fourier plane) of the collection objective. More details on the set-up and the measurement procedures are provided in Supplementary Section 6.

Numerical calculation of $P_{\mathrm{SHG}}(R, \omega, 2\omega)$. The SHG power $P_{\mathrm{SHG}}(R, \omega, 2\omega)$ in equation (1) consists of two contributions: the non-resonant scaling of the SHG $\propto \eta(\chi^{(2)}_{\mathrm{eff}}\omega)^2 N(R) I^2_\omega$ and the enhancement due to the resonances. The first part is retrieved via the numerical model described in Supplementary Section 8, by taking into account the specific features of $BaTiO_3$, that is, refractive indices and $\chi^{(2)}$ components, as well as the experimental size distribution of the nanocrystals. The RQPM properties of the SHG emerge as a result of the simulation and are not based on any prior assumption. The mean effective nonlinear tensor is also calculated independently $\chi^{(2)}_{\mathrm{eff}} = 28\,\mathrm{pm\,V^{-1}}$ according to Supplementary Section 8.2 in order to extract the proportionality constant $\eta = 1.19 \times 10^{-8}$ (mV pm s)^2 W^{-1} that accounts for other properties of the grains, such as the size distribution, refractive indices and birefringence. $\chi^{(2)}_{\mathrm{eff}}$ is frequency-independent since the working wavelengths are far from the $BaTiO_3$ bandgap (≈ 3.2 eV)[1].

The second part of $P_{\mathrm{SHG}}(R, \omega, 2\omega)$ is the volume-averaged squared field enhancement $\overline{\xi^2}$. The calculation of this factor requires the spatial distribution of the electric field enhancement within the microsphere, which is the ratio between the internal electric field and the electric field of the illumination. These are calculated in the EMM approximation for each specific R and for each value of ω and 2ω. The Mie modes were computed numerically with the Mie analytical solution for the internal fields (more details are given in Supplementary Section 5.2). The presence of the substrate was modelled with an absorption coefficient.

Data availability

The data that support the plots within this paper and other findings of this study are available from the corresponding author upon reasonable request.

Code availability

The codes that support the findings of this study are available from the corresponding author upon reasonable request.

Acknowledgements

We acknowledge discussions with M. Lehner, C. Renaut, V. Vogler-Neuling and L. Pattelli. We acknowledge support from the FIRST—Center for Micro and Nanoscience of ETHZ and from the Scientific Center of Optical and Electron Microscopy (ScopeM) of ETHZ. The project has received funding from the European Union's Horizon 2020 research and innovation programme under the Marie Skłodowska-Curie grant agreement no. 800487 (SECOONDO) and from the European Research Council under the grant agreement no. 714837 (Chi2-nano-oxides). We thank the Swiss National Science Foundation (SNF) grant 150609.

Author contributions

R.S. and R.G. conceived the work. R.S., M.Z. and L.I. developed the assembly method. R.S., A.M., F.K. and M.R.E. realized the structures, performed the FIB cuts and the SEM characterization. A.M., J.S.M. and F.T. performed the simulations. R.S., A.M. and J.S.M. developed the theory. R.S., A.M., J.S.M. and R.G. analysed the data. R.S. wrote the first draft of the manuscript. All authors discussed the results and contributed to the writing of the manuscript.

Competing interests

The authors declare no competing interests.

Additional information

Supplementary information is available for this paper at https://doi.org/10.1038/s41566-020-00701-x.

Correspondence and requests for materials should be addressed to R.S.

Reprints and permissions information is available at www.nature.com/reprints.